Experimental and computational investigation of weathering steel Q450NQR1 under high cycle fatigue loading via crystal plasticity finite element method

Tao Cong [a], Ruiyang Li [b], Zhanguang Zheng [b], Xianfeng Ma [c,*], Si Wu [a], Ruiqi Zhang [d], Filippo Berto [e], Jingyu Sun [f,*], Guian Qian [f,*]

[a] *Metals & Chemistry Research Institute, China Academy of Railway Sciences Corporation Limited, Beijing 100081, China*
[b] *College of Mechanical Engineering, Guangxi University, Nanning 530004, China*
[c] *Sino-French Institute of Nuclear Engineering and Technology, Sun Yat-Sen University, Zhuhai 519082, Guangdong, China*
[d] *Angang Steel Company Limited, Anshan 114021, China*
[e] *Department of Mechanical and Industrial Engineering, Norwegian University of Science and Technology (NTNU), Richard Birkelands vei 2b, 7491 Trondheim, Norway*
[f] *State Key Laboratory of Nonlinear Mechanics (LNM), Institute of Mechanics, Chinese Academy of Sciences, Beijing 100190, China,*

ARTICLE INFO

ABSTRACT

The fatigue properties of the Q450NQR1 steel were experimentally and computationally investigated. The experimental results show a large scatter of the fatigue lifetime under the high cycle fatigue loading. Based on the Voronoi diagram and crystal plastic model, a polycrystalline representative volume element (RVE) model with a pore or inclusion was constructed to analyze the effect of local stress–strain on the high cycle fatigue (HCF) and very-high-cycle fatigue (VHCF) life. Computational results show that the large deformation mostly occurs at the grain with a large Schmid factor. The increment of the mean accumulated plastic strain of the critical grain was proposed as the fatigue indicator parameter (FIP). A fatigue model was suggested based on the FIP, and the fatigue model can describe the influence of the material microstructures on fatigue life. The fatigue life curve with different sizes of defects was plotted and it is found that inclusions are the major factor in fatigue life dispersion.

1. Introduction

High-strength weathering steel is low-alloy steel with excellent atmospheric corrosion resistance made by adding a certain amount of alloying elements such as Cu, P, Cr, and Ni to the steel. Its good corrosion resistance can reduce the degradation of mechanical properties caused by corrosion during service. Q450NQR1 steel is a popular weathering steel that is used extensively in high-speed train structures, where the service environment is not always ideal, such as the wheel stick–slip and the resulting flats, which results in corresponding cyclic loads [1]. Its fatigue life has a significant impact on the safety of high-speed trains. The effect of three different surface defects on the fatigue strength of high-speed railway axles was investigated by means of experiments by Gao et al. [2]. However, the method cannot quantify the effect of material microstructure (grain size, inclusions, pores, etc.) on fatigue life.

Fatigue failure of steels under cyclic loading is divided into three stages, starting with microcrack nucleation due to inhomogeneous plastic deformation or grain boundary disruption, followed by crack propagation, and finally crack coalescence leading to rapid crack expansion. Under high cycle fatigue loading conditions, the fatigue failure was determined by the microcracks nucleation and expansion. These microcracks are usually several grains long and influenced by the local microstructure (grain size, weave, defects, etc.). Therefore, the randomness of fatigue behavior is often associated with changes in the local microstructure [3].

Depending on the development of experimental techniques and computational simulations in the last decades, the mechanism of fatigue failure was deeply studied. Dislocation theory has been widely accepted and used to explain the evolution of damage by analyzing the nucleation and expansion of microcracks under cyclic loading. With the development of dislocation theory, the crystal plastic model is established based on the crystal dislocation slip, which reflects the deformation

---

mechanism of crystalline materials and is consistent with the mechanical behavior of crystals [4]. Currently, crystal plastic finite element (CPFE) simulations are widely used to study the mechanical behavior of crystalline materials sensitive to microstructure, especially fatigue properties [5-8]. For example, Briffod et al. [9] investigated the effect of crystal morphology and rolling texture on fatigue crack initiation in BCC polycrystals using the fatigue indicator parameter (FIP) on the critical surface to quantify the susceptibility of microstructure on fatigue crack initiation. Zhang et al. [10] investigated the effect of building directions in additive manufactured AlSi10Mg on its high-cycle fatigue and very-high-cycle fatigue performance by using the CPFE simulations. It is concluded that the accumulated plastic strain influenced the HCF lifetime. Ye et al. [11] performed in-situ experiments and CPFE simulations to systematically investigate the location of slip bands and crack initiation points at the microscopic scale and the simulation results matched the experimental results very well. Similarly, Schafer et al. [12] used parameters to quantify the fatigue crack nucleation behavior with different microstructural defects.

The combination of representative volume element (RVE) and CPFE method is a powerful approach to study the crack initiation and expansion within the framework of computational micromechanics [13-20]. Gaur et al. [21] constructed a 2D crystalline RVE model using crystal parameters measured by electron backscatter diffraction (EBSD) to simulate the effects of mean stress and defects on the fatigue properties of aluminum alloys under cyclic loading. Cheong et al. [22] studied the cracks inside a 4-point bending specimen with the CPFE method under high cycle fatigue loading, and their model predicted the crack initiation correctly. Navarro et al. [23] compared the computational results of fatigue life between 2D and 3D models. They concluded that the 3D model provided better results, but the 2D model also produced results similar to the experiments.

Two methods are usually used in the RVE model generation: one is mapping the EBSD data to a regular finite mesh [21] and the other is generating a statistic type Voronoi tessellation considering grain size distribution [10]. The regular meshed RVE model of polycrystals contains steps and corners along grain boundaries which are physically unrealistic and inaccurate since the mechanical properties of grain boundaries are very much dependent on both local misorientations and the grain boundary plane's normal vector direction. Therefore, in the present work, a Voronoi tessellation was generated to study the fatigue behavior of Q450NQR1 steel under HCF and VHCF loadings.

The purpose of the present work is to try to relate material microstructure to fatigue life with the help of the crystal plasticity model. In the following sections, we will analyze the fatigue life of Q450NQR1 both experimentally and computationally.

2. Experiments

2.1. Material and specimen

The high-strength weathering steel Q450NQR1 investigated in the present study was provided by Angang Steel Company Limited. The Q450NQR1 steel is a body-centered-cubic structure (BCC) with a carbon (chemical) content of 0.062%. The detailed chemical composition of the steel is listed in Table 1 (see Table 2).

Fig. 1 depicts the initial microstructure of the Q450NQR1 steel. The EBSD diagram shows an isotropic grain distribution of the steel with an average grain size of 8.4 μm. The specimen was machined from a round bar and its dimension was shown in Fig. 2. The gauge length of the specimen is 20 mm and the diameter of the gauge section is 6 mm. The

Table 2
The material parameters of the crystal plasticity model.

Material parameters	Slip system {110} ⟨111⟩	Slip system {211} ⟨111⟩
Elastic constants C11, MPa	233,000	233,000
Elastic constants C12, MPa	135,000	135,000
Elastic constants C44, MPa	118,000	118,000
Reference strain rate $\dot{a}$, s^{-1}	0.001	0.001
n	20	20
K, MPa	205	510
Kinematic hardening, c_1	100	150
Kinematic hardening, c_2	3	3
Isotropic hardening, b	1	1
Isotropic hardening, Q, MPa	100	100

geometry fulfills the requirement of the ASTM standard E606. The outer surface of the specimen was polished in the axial direction to reduce the influence of surface roughness on the fatigue life.

2.2. Fatigue test

Both tensile and fatigue tests were performed on the MTS 810 servo-hydraulic testing machine. Fatigue tests were carried out in triangular waveform controlled by axial force with loading ratio R = -1.

Fig. 3 shows the S-N data of the investigated Q450NQR1 steel. The stress amplitudes of the fatigue tests were 360 MPa, 380 MPa, 390 MPa, 400 MPa, 410 MPa, and 420 MPa. The fatigue life increases as the stress amplitude decrease. The two testing results at the loading cycle 1×10^9 were run-out points. It is seen that the fatigue life increases as the stress amplitude decreases. The cracks under the VHCF loadings were mainly initiated at the interior or subsurface of the specimen. The characteristic of the crack initiation positions were facets and inclusions. From the S-N diagram, it can be observed the fatigue lives under the same stress amplitude representing a large dispersion, such as at the stress amplitude 420 MPa, the maximum difference of the fatigue life was about 30 times. The scatter of the fatigue lifetime was induced by the microstructure and inclusions of the material. In the next section, the crystal plasticity model was generated to investigate the phenomenon.

3. Computations

3.1. Crystal plasticity model

The crystal plasticity model was derived in a finite strain framework by the classical multiplication decomposition of the deformation gradient,

$$\mathbf{F} = \mathbf{F}^e \mathbf{F}^p, \tag{1}$$

where $\mathbf{F}^e$ is the elastic component of the deformation gradient and $\mathbf{F}^p$ denotes the plastic component of the deformation gradient. The rate of change of $\mathbf{F}^p$ is related to the slipping rate of the slip system by,

$$\dot{\mathbf{F}}^p (\mathbf{F}^p)^{-1} = \sum_{\alpha=1}^{N} \dot{\gamma}^{(\alpha)} \mathbf{m}^{(\alpha)} \otimes \mathbf{n}^{(\alpha)}, \tag{2}$$

where $\dot{\gamma}^{(\alpha)}$ is the slip rate of the α-th slip system, N is the total number of the slip systems, $\mathbf{m}^{(\alpha)}$ and $\mathbf{n}^{(\alpha)}$ are the slip direction and norm of the α-th slip plane, respectively. The velocity gradient is defined as,

$$\mathbf{L} = \frac{\partial \mathbf{v}}{\partial \mathbf{x}} = \frac{\partial \mathbf{v}}{\partial \mathbf{X}} \frac{\partial \mathbf{X}}{\partial \mathbf{x}} = \dot{\mathbf{F}} \mathbf{F}^{-1} = \mathbf{D} + \mathbf{\Omega}, \tag{3}$$

Table 1
Chemical composition of the steel Q450NQR1 (%).

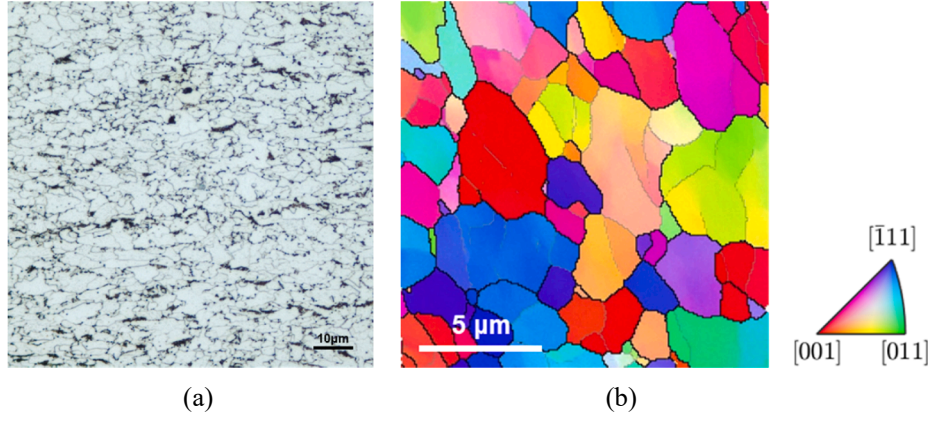| C	Si	Mn	P	S	Cu	Nb	Cr	Ni
0.062	0.261	1.012	0.013	0.001	0.296	0.026	0.173	0.186

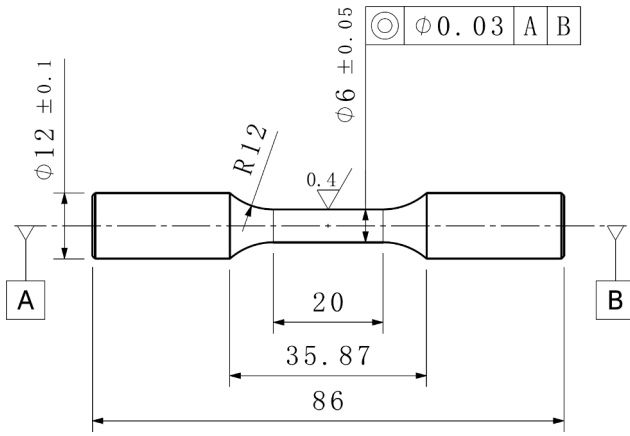**Fig. 1.** (a) Metallograph and (b) EBSD inverse pole figure (IPF) maps of the Q450NQR1 steel.
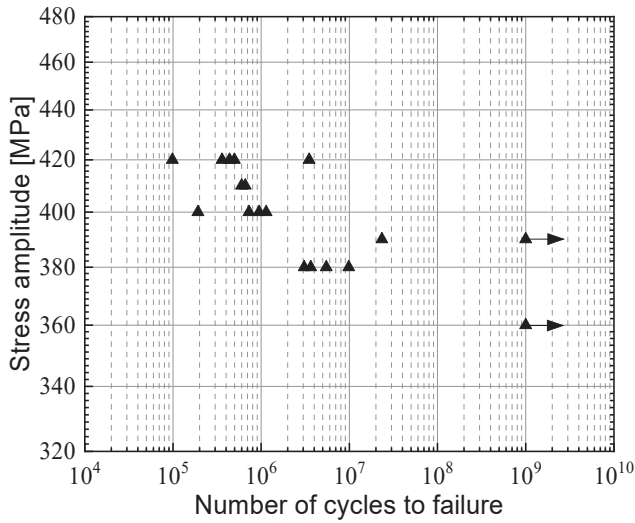

Fig. 2. Dimensions of the specimen.

Fig. 3. S-N data of Q450NQR1 steel with stress ratio $R = -1$.

where $\mathbf{m}^{*(\alpha)} = \mathbf{F}^e \mathbf{m}^{(\alpha)}$ and $\mathbf{n}^{*(\alpha)} = \mathbf{n}^{(\alpha)} (\mathbf{F}^e)^{-1}$ are the slip direction and norm in the deformed configuration. Assuming that the elastic deformations of the crystal are not affected by the sliding deformation, the constitutive relationship can be written as

$$\hat{\boldsymbol{\sigma}} = \mathbb{C} : \mathbf{D} - \sum_N^{\alpha=1} \left(\mathbb{C} : \mathbf{P}^{(\alpha)} + \boldsymbol{\Omega}^{(\alpha)} \cdot \boldsymbol{\sigma} - \boldsymbol{\sigma} \cdot \boldsymbol{\Omega}^{(\alpha)} \right) \dot{\gamma}^{(\alpha)} \tag{5}$$

where $\hat{\boldsymbol{\sigma}}$ is the Jaumann rate of Cauchy stress, $\mathbb{C}$ is the elastic moduli tensor. $\mathbf{P}^{(\alpha)}$ and $\boldsymbol{\Omega}^{(\alpha)}$ are determined by

$$\mathbf{P}^{(\alpha)} = \frac{1}{2} \left(\mathbf{m}^{*(\alpha)} \otimes \mathbf{n}^{*(\alpha)} + \mathbf{n}^{*(\alpha)} \otimes \mathbf{m}^{*(\alpha)} \right), \tag{6}$$

$$\boldsymbol{\Omega}^{(\alpha)} = \frac{1}{2} \left(\mathbf{m}^{*(\alpha)} \otimes \mathbf{n}^{*(\alpha)} - \mathbf{n}^{*(\alpha)} \otimes \mathbf{m}^{*(\alpha)} \right). \tag{7}$$

Based on Schmid's law, the slipping rate $\dot{\gamma}^{(\alpha)}$ on the α-th slip system is corresponding to the Schmid stress $\tau^{(\alpha)}$. The flow rule is suggested using a power law as:

$$\dot{\gamma}^{(\alpha)} = \dot{a} \left\langle \frac{\left| \tau^{(\alpha)} - \alpha^{(\alpha)} \right| - r^{(\alpha)}}{K} \right\rangle^n \mathrm{sign} \left(\tau^{(\alpha)} - \alpha^{(\alpha)} \right), \tag{8}$$

where $\alpha^{(\alpha)}$ is the back stress, $\dot{a}$ is the reference strain rate, K and n are the material constants, and $r^{(\alpha)}$ is the isotropic hardening term. The rate of backstress $\alpha^{(\alpha)}$ was proposed as:

$$\dot{\alpha}^{(\alpha)} = c_1 \dot{\gamma}^{(\alpha)} - c_2 \left| \dot{\gamma}^{(\alpha)} \right| \alpha^{(\alpha)}. \tag{9}$$

The evolution of isotropic hardening variable $r^{(\alpha)}$ is suggested as:

$$\dot{r}^{(\alpha)} = bQ \sum_\beta h_{\alpha\beta} \left(1 - b\rho^{(\beta)} \right) \left| \dot{\gamma}^{(\beta)} \right|. \tag{10}$$

The internal state variable $\rho^{(\alpha)}$, which represents the dislocation hardening, is defined by:

$$\dot{\rho}^{(\alpha)} = \left(1 - b\rho^{(\alpha)} \right) \left| \dot{\gamma}^{(\alpha)} \right|. \tag{11}$$

where c_1, c_2, b, Q are material constants.

3.2. Finite element model

The 2D finite element RVE model of the investigated steel is shown in Fig. 4. Both the height and the width of the model are 200 μm. The polycrystalline grain structure was generated by the open-source software Neper based on Voronoi tessellation. Fig. 5 shows the grain size distribution of the Voronoi tessellation. The average grain size is 8.4 μm which is approximated to the experiment results. The tessellation
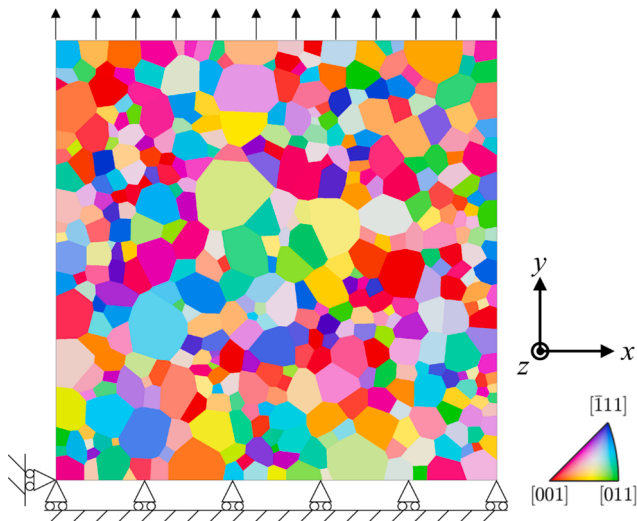
where $\mathbf{D}$ is the symmetric part and $\boldsymbol{\Omega}$ is the antisymmetric spin tensor of the velocity gradient $\mathbf{L}$. The plastic component of the velocity gradient is given by,

$$\mathbf{L}^p = \mathbf{F}^e \dot{\mathbf{F}}^p (\mathbf{F}^p)^{-1} (\mathbf{F}^e)^{-1} = \mathbf{F}^e \sum_N^{\alpha=1} \dot{\gamma}^{(\alpha)} \mathbf{m}^{(\alpha)} \otimes \mathbf{n}^{(\alpha)} (\mathbf{F}^e)^{-1} = \sum_N^{\alpha=1} \dot{\gamma}^{(\alpha)} \mathbf{m}^{*(\alpha)} \otimes \mathbf{n}^{*(\alpha)} \tag{4}$$

Fig. 4. Tessellation of the Voronoi model.

Fig. 5. Grain size distribution of the Voronoi model.

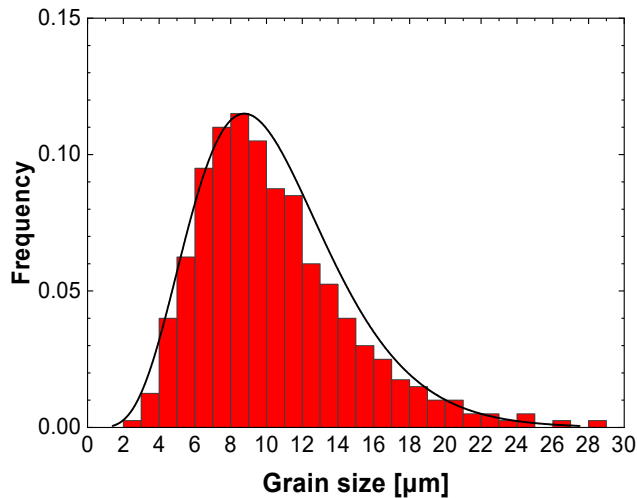**Fig. 6.** Pole figures of (a) ⟨1 0 0⟩, (b) ⟨1 1 1⟩ orientation for the crystallographic orientations of the Voronoi model.

contains 400 grains. The four-node plane strain element is used to mesh the model, and the total number of elements is about 25000. To avoid rigid body motion, the node in the bottom-left corner was limited in the *x* and *y* directions in Fig. 4. All nodes at the bottom were fixed in the *y*-direction. The boundary on the left and right sides is periodic. At a strain rate of 0.001 s⁻¹, a uniaxial load was applied at the upper border of the model along the vertical (*y*-axis) direction to simulate uniaxial tensile tests.

Corresponding to the experimental results, the isotropic texture is used in the present model. The grain orientations were generated randomly. Fig. 6 shows that the crystallographic of the model has no preferential orientations. A set of Euler angles is used to specify the 3D orientation of each grain concerning the specimen axes.

To investigate the effects of defects, i.e., holes and inclusions, on the fatigue behavior of the high-strength weathering steel, the Voronoi aggregate model with a hole or inclusion was built. As shown in Fig. 7 (a), there is a hole with a diameter of 20 μm at the center of the model. Regarding the effect of inclusion, the model with inclusion was generated, as shown in Fig. 7(b). A circular inclusion with a diameter of 20 μm was surrounded by multiple grains. The dimension came from the statistical average value from experimental micrographs. According to the experimental characterization by scanning electron microscopy (SEM)
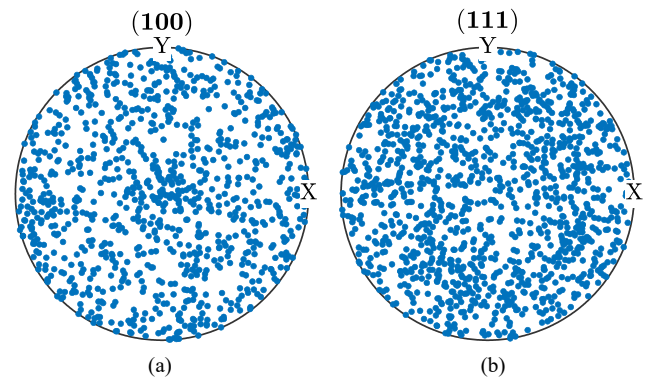
and energy dispersive spectrometer (EDS) analyses, the inclusions in the steel alloy are mainly CaO·Al₂O₃, with elastic modulus $E = 370$ GPa and Poisson ratio $\mu = 0.22$. There was no evident interfacial gap between the inclusion and the base material. Hence the inclusion is assumed to be perfectly bonded with the matrix. Cyclic tension–compression load was applied at the upper boundary of the polycrystal finite element model along the vertical (y-axis) direction with the stress ratio $R = -1$, as shown in Fig. 4.

3.3. Parameters of the crystal plastic model

To evaluate the mechanical and fatigue properties of the investigated high-strength weathering steel, the simulations, under tensile and cyclic tension–compression loading conditions, were conducted using the software ABAQUS with a user-defined material subroutine (UMAT) program based on crystal plasticity theory introduced in Section 3.1. The high-strength weathering steel alloy has a body center cubic (BCC) structure. Hence, the possible slip systems are {1 1 0}⟨1 1 1⟩, {1 1 2}⟨1 1 1⟩ and {1 2 3} ⟨1 1 1⟩. According to [24-26], the {1 1 0}⟨1 1 1⟩ and {1 1 2}⟨1 1 1⟩ slip systems can be activated at room temperature, while the slip at {1 2 3}⟨1 1 1⟩ only occurs at high temperature. Therefore, only the {1 1 0}⟨1 1 1⟩ and {1 1 2}⟨1 1 1⟩ slip systems are implemented in the present model.

The strain rate was kept at 0.001 s⁻¹ in the simulation as well as in the experiment. Fig. 8 shows the engineering stress–strain curve obtained using these boundaries for a 2D microstructure with randomly oriented grains (no texture) under plane strain conditions. The figure illustrates that parameters of the constitutive model can be selected to conform to the experimentally measured stress–strain curve. Material parameters used in the crystal plasticity model are shown in Table 1. The model neglected the stage of the yield-point elongation.

4. Results and discussions

4.1. Computational results with no defect

Fig. 9 shows the distribution of axial strain and axial stress of the Voronoi model under uniaxial tensile. Obvious shear bands due to crystal slip were observed in Fig. 9(a). When the nominal strain of the RVE model is 1%, the maximum local axial strain is 4.7%. As the nominal strain of the RVE model achieves 5%, the maximum local axial strain becomes 24.8%. The local stress concentration was caused by the non-uniformity of material microstructure.

In the study, the grain orientations were generated randomly. Due to the random orientations of the grains, grain boundaries are associated with a range of misorientation angles. The grain boundaries misorientation angle can be calculated from the orientation matrix **g**, which is defined as
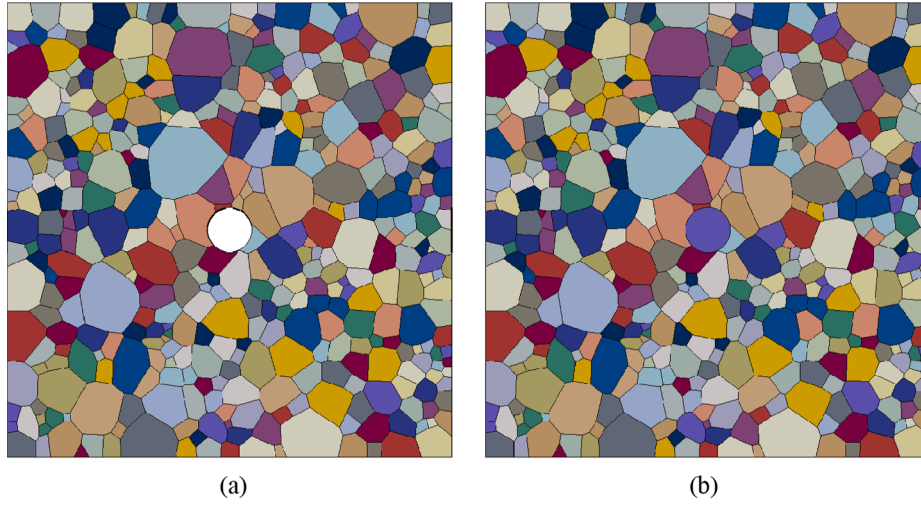
(a)

(b)

Fig. 7. (a) Tessellation with a hole. (b) Tessellation with an inclusion.

$$\mathbf{g} = \begin{bmatrix} \cos\Phi_1\cos\Phi_2 - \sin\Phi_1\sin\Phi_2\cos\Phi & \sin\Phi_1\cos\Phi_2 + \cos\Phi_1\sin\Phi_2\cos\Phi & \sin\Phi_2\sin\Phi \\ -\cos\Phi_1\sin\Phi_2 - \sin\Phi_1\cos\Phi_2\cos\Phi & -\sin\Phi_1\sin\Phi_2 + \cos\Phi_1\cos\Phi_2\cos\Phi & \cos\Phi_2\sin\Phi \\ \sin\Phi_1\sin\Phi & -\cos\Phi_1\sin\Phi & \cos\Phi \end{bmatrix}, \tag{12}$$

where Φ_1, Φ_2 and Φ are Euler angles of the grain.

The misorientation matrix $\Delta\mathbf{g}$ at the grain boundaries can be obtained by

$$\Delta\mathbf{g} = \mathbf{g}_1 \cdot \mathbf{g}_2^{-1}, \tag{13}$$

where $\mathbf{g}_1$ and $\mathbf{g}_2$ are the orientation matrices of two neighboring grains. The misorientation angle θ is then calculated using the trace of the misorientation matrix via

$$\theta = \arccos[\operatorname{trace}(\Delta\mathbf{g})/2]. \tag{13}$$

The misorientation at the grain boundaries of the polycrystal model was calculated and plotted in Fig. 10(a). According to the symmetry of the BCC metal, the available grain boundary misorientations are in the range from 0° to 62.8°. Comparing Fig. 9 and Fig. 10 (a), the maximum
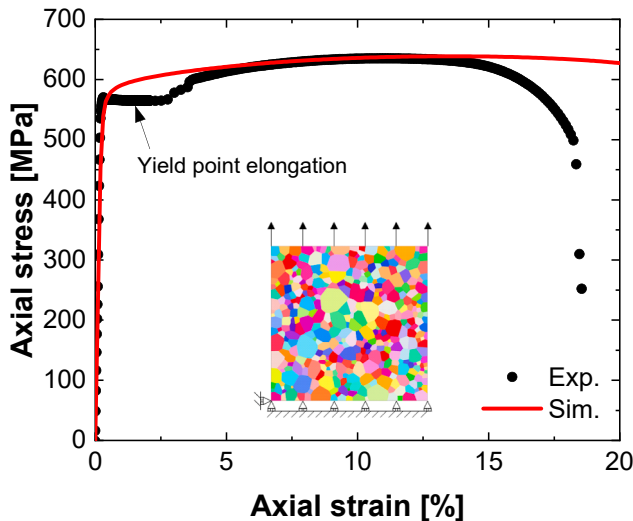
deformation usually occurs near the grain boundaries, corresponding to grain boundary angles between 30° and 60°. The reason is that large angular grain boundaries are more susceptible to deformation incoherence resulting in local deformation concentration.

The Schmid factor for $\{1\,1\,0\}\langle 1\,1\,1\rangle$ slip system corresponding to the polycrystal model under vertical tension loading was shown in Fig. 10 (b). The blue line in each crystal is the intersection line of the slip plane and x-y plane, and the red arrow represents the projection of the slip direction on the x-y plane. According to Schmid's law, the greater the Schmid factor, the greater the effective critical resolved shear stress, and the corresponding slip system will be easily activated. Comparing Fig. 9 and Fig. 10 (b), it is observed that the shear band usually occurs in the grain with large Schmid factors.

We calculated the mean strain of each grain at the tensile load of 1% and 5% nominal strain. Fig. 11 shows the relation between the Schmid factor and mean strain. The vertical axis is the normalized axial strain $\varepsilon_y/\varepsilon_{y,\max}$. According to the symmetry of the BCC metal, the Schmid factor is distributed in the range of 0.3 to 0.5. The relative frequency of the grains' Schmid factors increases as the Schmid factor increases. Most of the Schmid factors of the grains are greater than 0.4 in the present multiple crystal model. The statistical charts at the right side of Fig. 11 show the axial strain distribution of the whole Voronoi model. It is found most of the grains were less deformed. However, grains with large mean strain were also existed, mainly in grains with Schmid factors close to 0.5. The relative frequency of normalized axial strain follows the Weibull distribution. As the tensile load from 1% to 5%, the center of the distribution moves upwards, which means the number of grains entering the plastic zone increases.

Cyclic loading was performed on the no defects RVE model to investigate the cyclic plastic behavior of the Q450NQR1 steel. The stress–strain hysteresis curves under different strain amplitudes by crystal plasticity simulation are shown in Fig. 12. The material shows a cyclic hardening behavior. As the number of cycles increases, the hysteresis loop gradually tends to stabilize. According to the assumptions of the proposed crystal plasticity model, there is a saturation value for the isotropic hardening of the material. As shown in Eq. (10), the magnitude of the saturation value is Q, and parameter b controls the rate at which
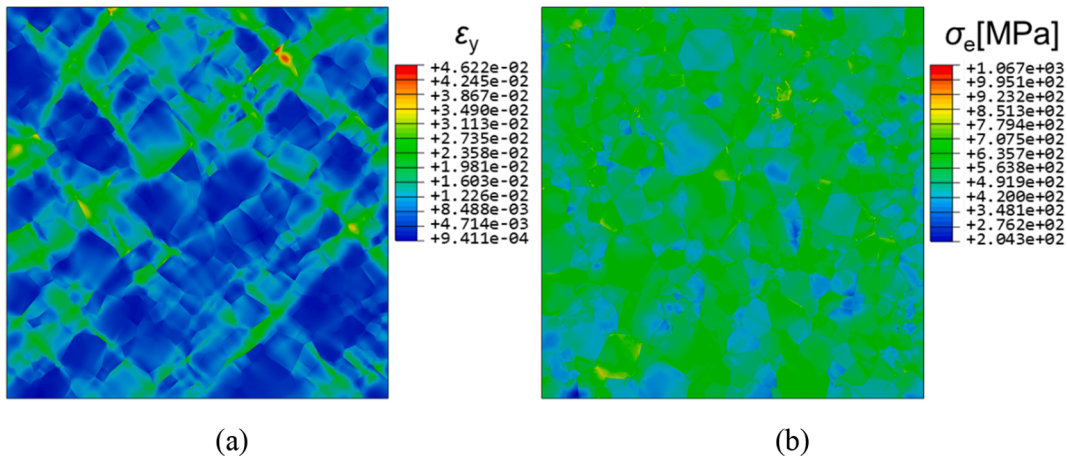

Fig. 8. Comparison of experimental and computational results.

Fig. 9. Computational results of (a) axial strain and (b) Mises stress under the uniaxial tensile.
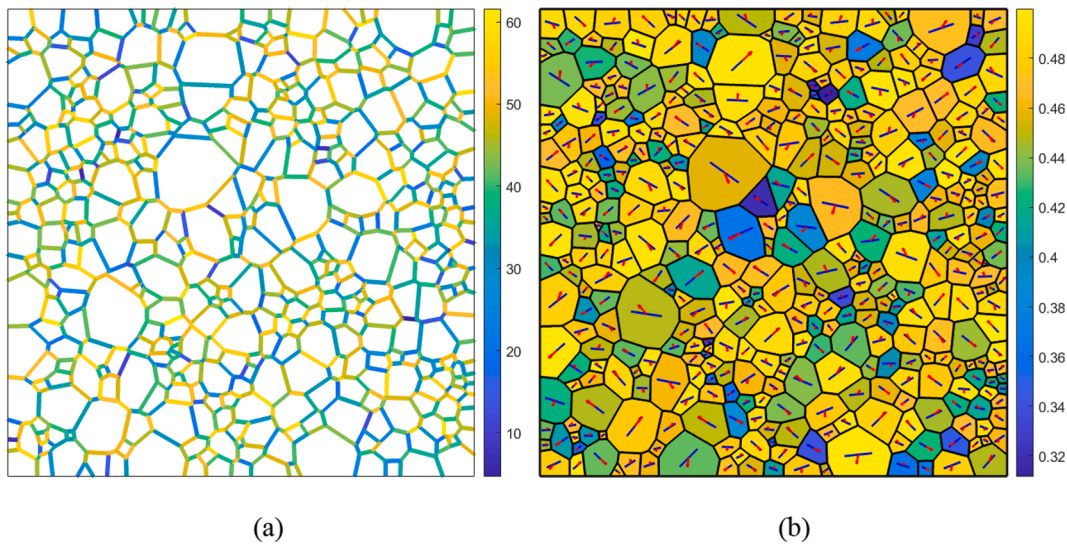
Fig. 10. (a) Misorientation of the Voronoi model and (b) the Schmid factor of $\{1\,1\,0\}\langle1\,1\,1\rangle$ slip system under vertical tensile loading.
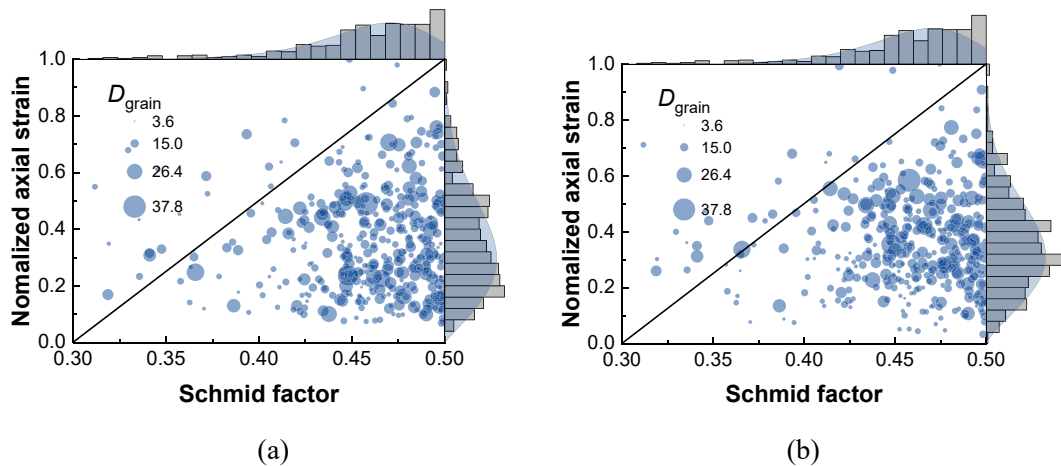

Fig. 11. Schmid factor vs. grain mean strain at the axial nominal strain (a) 1% and (b) 5%.

the saturation value is reached. The crystal plasticity calculation is time-consuming. Considering the computational cost, all numerical calculations in this study were stopped after the steady-state was reached.

Fig. 13 shows the computational results of fatigue tests with the RVE model. The figures of Mises stress σ_e, axial strain ε_y are plotted at the maximum tensile stress in the steady cycle. Compared with Fig. 9, the
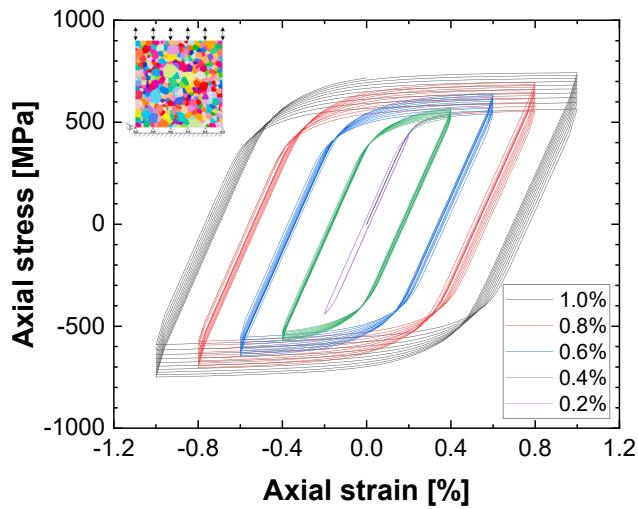
Fig. 12. The computed cyclic stress–strain curves of Q450NQR1 steel under different strain amplitudes.

locations of the maximum Mises stress are different from the monotonic tensile simulations, as well as the axial strain. Under the cyclic loading, the plastic hardening leads to an increase in the yield strength of the grains, and the global stress distribution is reallocated according to the deformation coordination conditions.

The accumulated plastic shear strain p_{ac} is defined as:

$$p_{ac} = \int_0^t \sqrt{\frac{2}{3}\mathbf{L}_p : \mathbf{L}_p} d\tau. \tag{14}$$

From the CPFE simulation, it was found that the maximum p_{ac} could be attributed to the presence of a critical soft-hard-soft grain combination, characterized by high normal stress on the basal plane of the hard grain and significantly higher basal and prismatic slip activities in the adjacent soft grains.

4.2. Computational results with pores and inclusions

The FE models with a pore of 20 μm and inclusion of 20 μm are shown in Fig. 7. To study the influence of the defect size on the fatigue life, the FE models with different diameter pores and inclusions were built. Their diameters were 20 μm, 40 μm, 60 μm, 80 μm, 100 μm. The defect sizes and stress amplitudes of the simulations are listed in Table 3. The centers of the pores and inclusion are located at the shape center of

Table 3
Dimensions of defects and boundary conditions of the simulation.

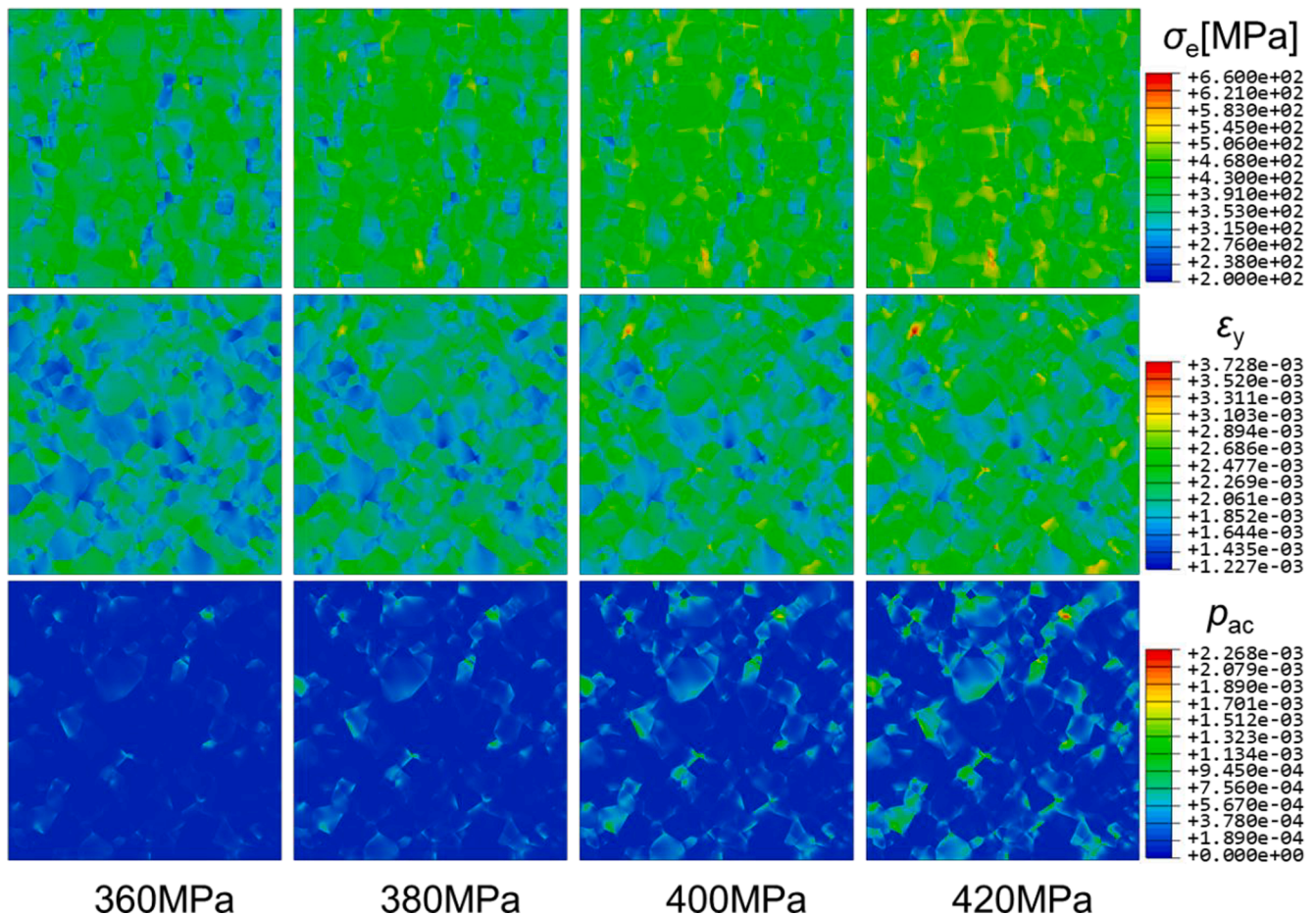| Stress amplitude [MPa]	Diameter of the hole [μm]	Diameter of the inclusion [μm]
203	20, 40, 60, 80, 100	–
360	20, 40, 60, 80, 100	20, 40, 60, 80, 100
380	20, 40, 60, 80, 100	20, 40, 60, 80, 100
400	20, 40, 60, 80, 100	20, 40, 60, 80, 100
420	20, 40, 60, 80, 100	20, 40, 60, 80, 100
609	20, 40, 60, 80, 100	–

Fig. 13. Mises stress σ_e, axial strain ε_y and accumulated plastic strain p_{ac} at the steady cycle under the fatigue loadings of ±360 MPa, ±380 MPa, ±400 MPa, ±420 MPa.
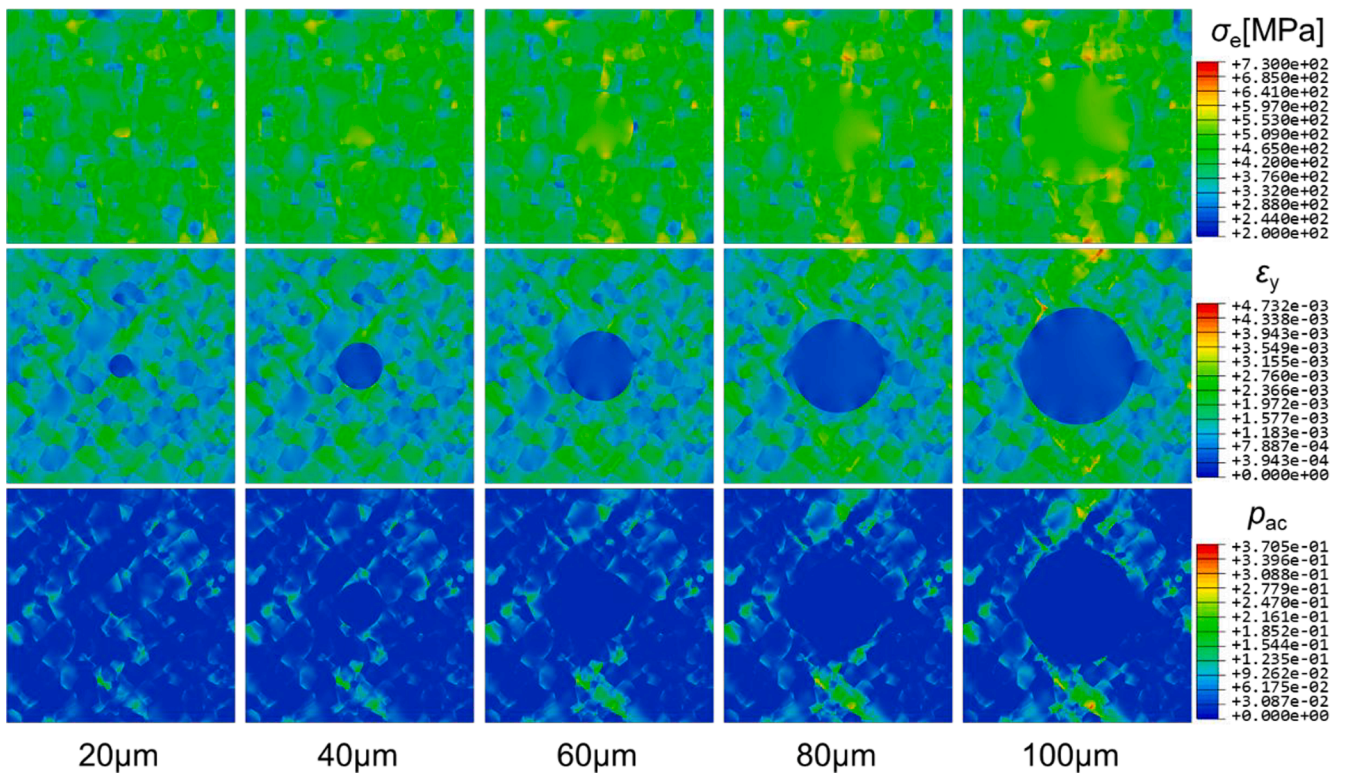
Fig. 14. Mises stress σ_e, axial strain ε_y and accumulated plastic strain p_{ac} at the steady cycle under the fatigue loadings of ±420 MPa, with inclusion diameters of 20 μm, 40 μm, 60 μm, and 80 μm, 100 μm.

the RVE model. Fig. 14 shows the computational results at the steady cycle under the fatigue loadings of ±420 MPa, with inclusion diameters of 20 μm, 40 μm, 60 μm, and 80 μm, 100 μm. Inclusions are only

deformed elastically at the current stress level. Therefore, in the diagram of the distribution of axial strain ε_y, the inclusions are low strain regions and there is a significant discontinuous interface between the inclusions
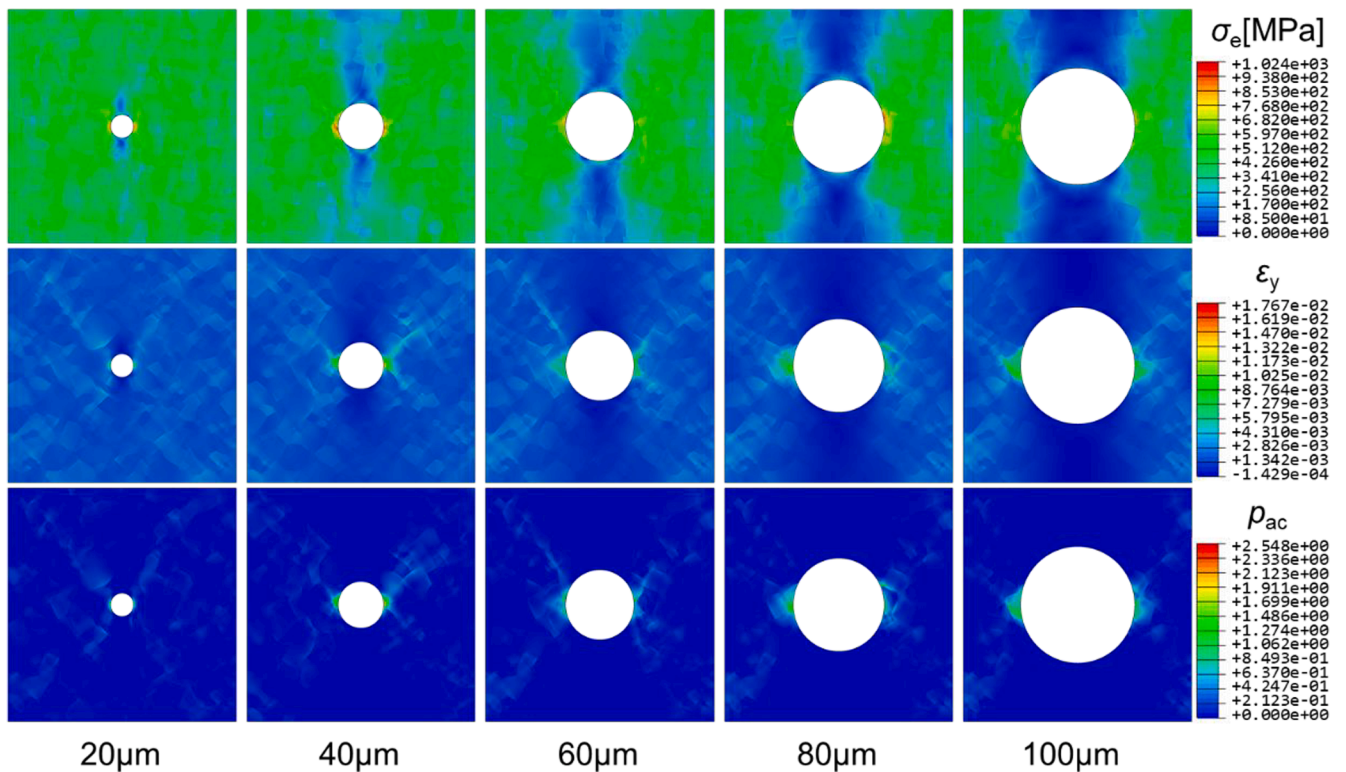

Fig. 15. Mises stress σ_e, axial strain ε_y and accumulated plastic strain p_{ac} at the steady cycle under the fatigue loadings of ±420 MPa, with pore diameters of 20 μm, 40 μm, 60 μm, and 80 μm, 100 μm.

and the steel. However, we do not observe significant discontinuous interfaces of the Mises stress in Fig. 14. As the diameter of the inclusion increases, the maximum accumulated plastic strain p_{ac} of the RVE model increases. The location of the maximum p_{ac} do not occur at the interface of inclusions. The inclusions induced an increase in the cumulative plastic strain in the shear bands adjacent to them.

Fig. 15 shows the computational results at the steady cycle under the fatigue loadings of ±420 MPa, with inclusion diameters of 20 μm, 40 μm, 60 μm, and 80 μm, 100 μm. The location of maximum σ_e always occur at the surface of the pore. The maximum σ_e always occurs at the surface of the hole, and the position of the line with the center of the hole is perpendicular to the loading direction. The distribution of axial strain ε_y is similar, the strain near the top and bottom of the hole is the smallest, the strain in the area along the loading direction 45° is large, and the strain in the area near the left and right of the hole is the largest. The strain in the area to the left and right of the hole is the largest, and the radiation range is larger with the increase of the hole diameter. The accumulated plastic strain p_{ac} is mainly distributed in the slip zone near the hole, and the interaction reaches the maximum around the hole, while there is almost no plastic strain generated in other areas.

4.3. The accumulated plastic strain

The Voronoi model with a pore or inclusion was computed in the study with the crystal plastic model. The upper boundary of the Voronoi model was subjected to a cyclic tension–compression fatigue loading along the *y*-direction with a nominal stress amplitude of ±360, ±380, ±400, ±420 MPa.

Fig. 16 shows the variation of the accumulated plastic strain p_{ac} for CPFE polycrystalline models under cyclic tension–compression loadings with different stress amplitudes σ_a. It is evident that p_{ac} increases with the accumulation of loading cycles. And the larger the stress amplitudes σ_a is, the greater the plastic strain p_{ac} is. Additionally, defects can cause the increase of p_{ac}. According to the study of Gillner and Münstermann [27], the increment of local accumulated plastic shear strain kept almost constant after the initial several cycles. From Fig. 16 it is observed, after about 10 loading cycles, the changes of p_{ac} with the per loading cyclic enter a stable state.

From Fig. 17, it can be seen that the von Mises stress of each grain is approximately normally distributed, with the increase of the defect diameter, its average value almost does not change, but the distribution graph gradually becomes flat, that is, the standard deviation increases, reflecting the process of gradual dispersion of the von Mises stress distribution of each grain with the growth of the defect diameter. For a very large part of the grains, there is no plastic accumulation, and most of the grains with plastic accumulation are also gathered in a small range, but

there are still some grains with large cumulative plastic deformation. As the defect diameter gradually increases, the maximum cumulative plastic strain also gradually increases, and the data points become more and more discrete, but for the grains in the same cumulative plastic strain, their average stress changes are small.

4.4. Fatigue indicator parameter (FIP) and lifetime prediction

Manonukul [28] demonstrated that accumulated plastic strain is strongly related to the crack initiation process and can thus be utilized to calculate the fatigue crack initiation life under cyclic loads. Therefore, the location of the maximum accumulated plastic strain is the critical point of the RVE model. However, since the finite element method is a numerical solution to a system of partial differential equations, there may be some computational errors in the calculation results at the elements with large deformation gradients. Factors such as mesh density, mesh quality, and element type can have an impact on the calculation results. For the FE model in this study, if only the values of a single node are used for the life prediction, large errors may occur. Therefore, the mean accumulated plastic strain of each grain was calculated to reduce the influence of local deformation concentration on fatigue life calculation, and the critical grain was defined as the grain where the maximum mean p_{ac} is located, according to the critical distance method. The mean p_{ac} of the critical grain was denoted as $p_{ac,cg}$ which was obtained by

$$p_{ac,cg} = \max\left\{\frac{1}{V_i}\int_{V_i} p_{ac}\mathrm{d}v, i = 1, 2\cdots, n\right\},$$ (15)

where n is the total number of grains, V_i is the volume of the *i*-th grain.

In the study, we suggested that increment of $p_{ac,cg}$ in the stable loading cycles $\Delta p_{ac,cg}$ as the fatigue indicator parameter,

$$\mathrm{FIP} = \Delta p_{ac,cg} = p_{ac,cg}|_{N+1} - p_{ac,cg}|_N.$$ (16)

Fig. 18 shows the $\Delta p_{ac,cg}$ under different stress amplitudes with inclusions and pores. For the model without defect, all of the $\Delta p_{ac,cg}$ values are smaller than 0.001. All $\Delta p_{ac,cg}$ values with inclusions are in the range from 0.001 to 0.01. The $\Delta p_{ac,cg}$ increases as the stress amplitude increases, and the $\Delta p_{ac,cg}$ also increases as the inclusion diameter increases.

The relation between the FIP and the fatigue life N_f was given by a power law,

$$\mathrm{FIP} = A\left(N_f\right)^B,$$ (16)

where A and B are the model parameters.

The average size of the inclusions in the material is about 40 μm, so the computational results of the model with 40 μm inclusion were used
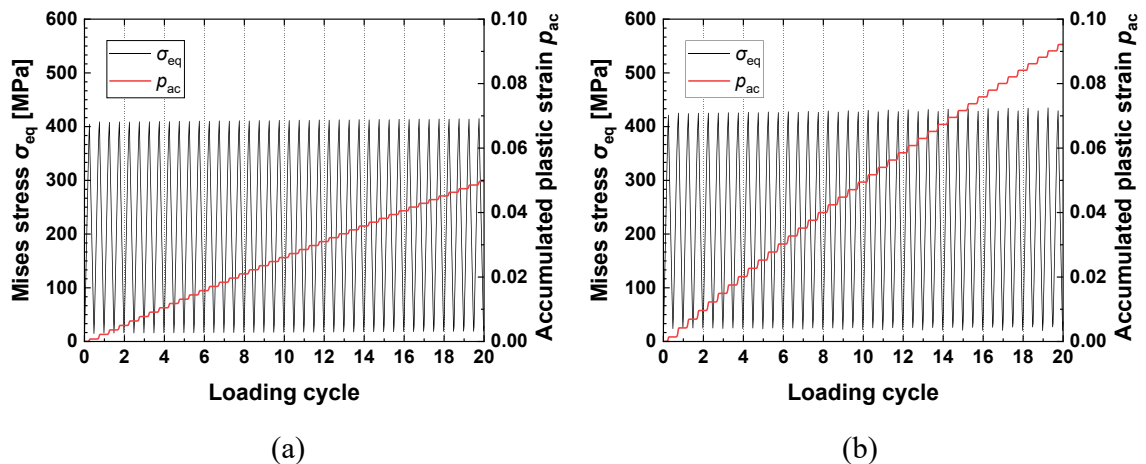

Fig. 16. Accumulated plastic strain and Mises stress under cyclic loading ±360 MPa with the inclusions diameter of (a) 40 μm and (b) 80 μm.
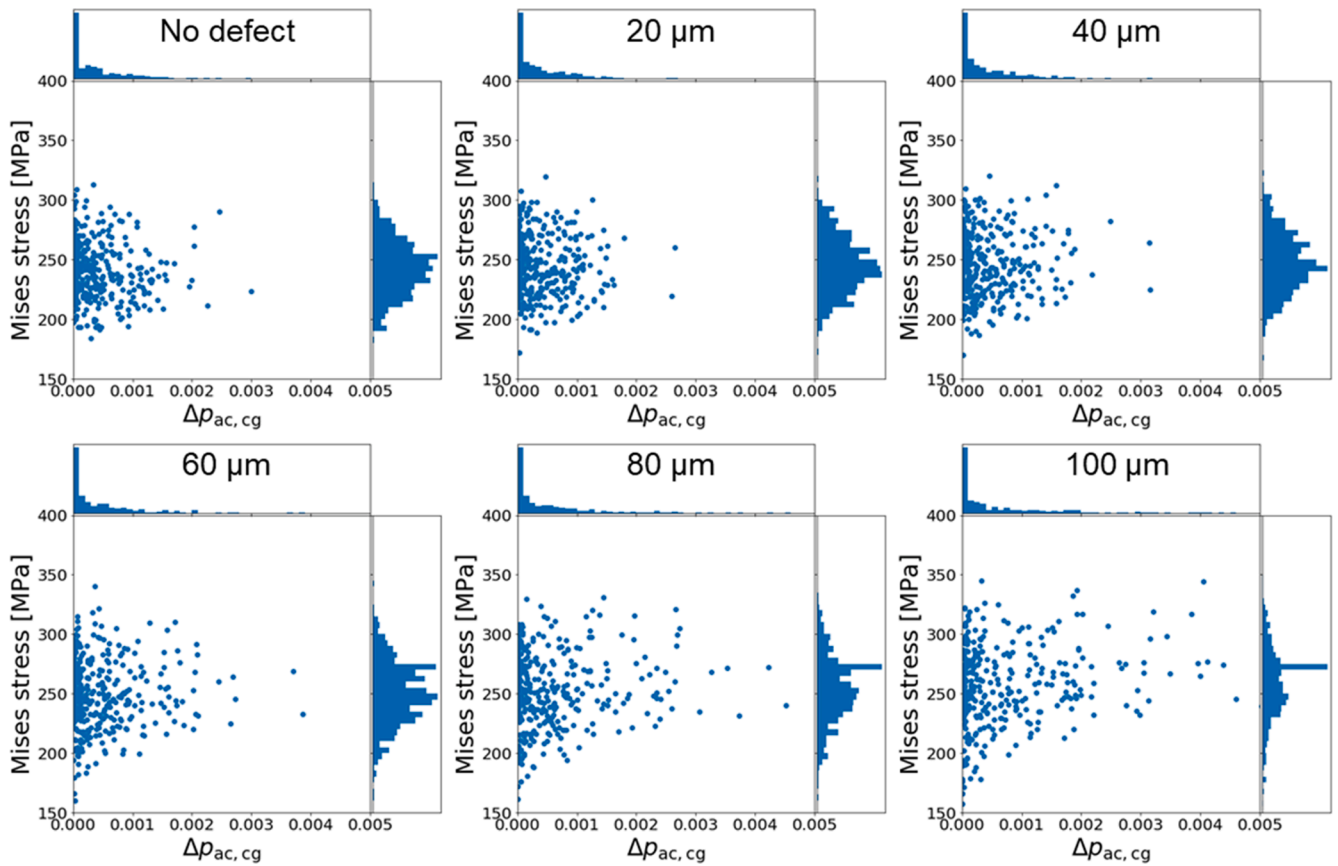
Fig. 17. Distributions of grain mean Mises stress and accumulated plastic strain increment $\Delta p_{ac,cg}$ in numerical models with the same microstructure configuration but different inclusion sizes.
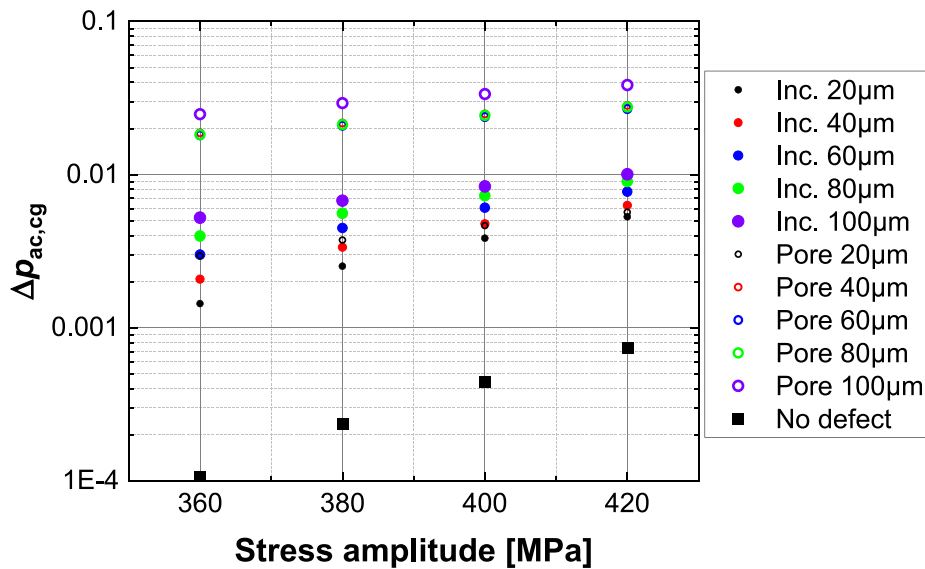

Fig. 18. Stress amplitude vs. $\Delta p_{ac,cg}$ with different dimensions of defects.

to fit the fatigue life. The model parameters were determined as $A = 0.12315$ and $B = -0.23246$. Therefore, the fatigue life can be predicted by

$$\ln(N_f) = 9.0095 - 4.3018\ln(\text{FIP}). \qquad (17)$$

Fig. 19(a) shows the predicted fatigue life with different diameters of inclusions and Fig. 19(b) shows the predicted results with different

diameters of pores. In Fig. 19(a), most of the fatigue life is located between the fatigue curves including 20 μm and 60 μm inclusions. In Fig. 19(b), the fatigue life decreases rapidly when the pore diameter is larger than 20 μm.

In the study, an attempt is made to explain the dispersion of material fatigue lifetime when it contains inclusions/pores by establishing a FIP based on the information of material microstructure with the crystal
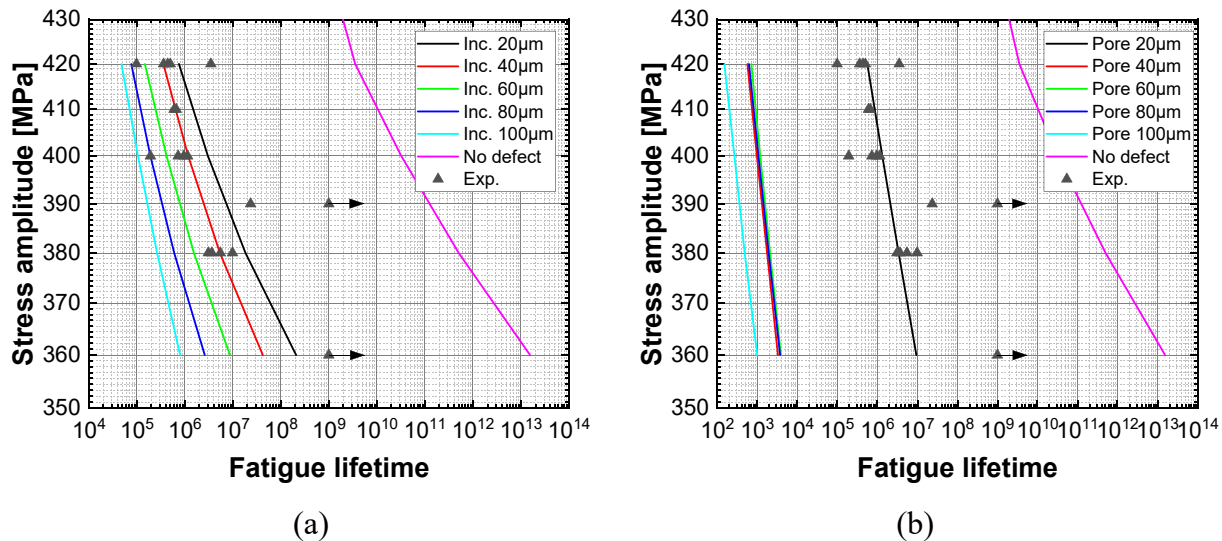
Fig. 19. Predicted fatigue lifetime with (a) inclusions and (b) pores.

plasticity model. The method proposed in the article provides a new perspective linking material microstructure to macroscopic fatigue performance.

The model proposed in this paper still has some limitations. In the present work, a two-dimensional RVE model is used, so it cannot describe the information of the grains in the third direction and is therefore limited to the use of isotropic materials. For three-dimensional structures, it is recommended to build the local RVE model in the plane corresponding to the first and second principal stresses, and when the third principal stress is small, the model in this paper can be seen as an approximation to the 3-dimensional case.

5. Conclusions

In the study, the Voronoi FE models with inclusions and pores were generated to simulate the local mechanical response of the weathering steel Q450NQR1 under tensile and (HCF, VHCF) fatigue loadings. The crystal plastic constitutive law was used to study the cyclic plasticity behavior of the steel. The following conclusions have been obtained:

(1) Obvious shear bands due to crystal slip were observed in the tensile and fatigue computations and the shear bands usually occur in the grains with large Schmid factors. There is a positive correlation between deformation and Schmid factor, and grains with large Schmid factors have a higher probability of large deformation.

(2) The local stress–strain distribution was influenced by the inclusions and pores and the accumulated plastic strain increased substantially at the boundary of defects. As a result, the crack initiation was accelerated, and the fatigue life was reduced. In addition, the calculations show that the effect of pores on the accumulated plastic strain of grains is more significant than the effect of inclusions.

(3) The increment of the critical grain's mean accumulated plastic strain was proposed as the fatigue indicator parameter. Based on the CPFE computational results, the fatigue model can predict the fatigue life of Q450NQR1 steel with different sizes of defects, which can describe the data dispersion found in the experiments.

The authors declare that they have no known competing financial interests or personal relationships that could have appeared to influence the work reported in this paper.

Declaration of Competing Interest

The authors declare that they have no known competing financial interests or personal relationships that could have appeared to influence

the work reported in this paper.

References

[1] Gao J-W, Yu M-H, Liao D, Zhu S-P, Han J, Lesiuk G, et al. Fatigue and damage tolerance assessment of induction hardened S38C axles under different foreign objects. Int J Fatigue 2021;149:106276. https://doi.org/10.1016/j.ijfatigue.2021.106276.

[2] Gao J-W, Dai G-Z, Li Q-Z, Zhang M-N, Zhu S-P, Correia JAFO, et al. Fatigue assessment of EA4T railway axles under artificial surface damage. Int J Fatigue 2021;146:106157. https://doi.org/10.1016/j.ijfatigue.2021.106157.

[3] Pineau A, Benzerga AA, Pardoen T. Failure of metals I: Brittle and ductile fracture. Acta Mater 2016;107:424–83. https://doi.org/10.1016/j.actamat.2015.12.034.

[4] Nguyen K, Zhang M, Amores VJ, Sanz MA, Montans FJ. Computational modeling of dislocation slip mechanisms in crystal plasticity: a short review. Crystals 11(1) (2021). doi: 10.3390/cryst11010042.

[5] Sinha S, Ghosh S. Modeling cyclic ratcheting based fatigue life of HSLA steels using crystal plasticity FEM simulations and experiments. Int J Fatigue 28(12) (2006) 1690–1704, doi: 10.1016/j.ijfatigue.2006.01.008.

[6] Guilhem Y, Basseville S, Curtit F, Stephan JM, Cailletaud G. Investigation of the effect of grain clusters on fatigue crack initiation in polycrystals. Int J Fatigue 2010;32(11):1748–63. https://doi.org/10.1016/j.ijfatigue.2010.04.003.

[7] Paulson NH, Priddy MW, McDowell DL, Kalidindi SR. Reduced-order microstructure-sensitive protocols to rank-order the transition fatigue resistance of polycrystalline microstructures. Int J Fatigue 2019;119:1–10. https://doi.org/10.1016/j.ijfatigue.2018.09.011.

[8] Wang J, Jiang W. Numerical assessment on fatigue damage evolution of materials at crack tip of CT specimen based on CPFEM. Theor Appl Fract Mech 2020;109: 102687. https://doi.org/10.1016/j.tafmec.2020.102687.

[9] Briffod F, Shiraiwa T, Enoki M. Numerical investigation of the influence of rolling texture and microstructure on fatigue crack initiation in BCC polycrystals. Int J Fatigue 2018;107:72–82. https://doi.org/10.1016/j.ijfatigue.2017.10.019.

[10] Zhang W, Hu Y, Ma X, Qian G, Zhang J, Yang Z, et al. Very-high-cycle fatigue behavior of AlSi10Mg manufactured by selected laser melting: Crystal plasticity modeling. Int J Fatigue 2021;145:106109. https://doi.org/10.1016/j.ijfatigue.2020.106109.

[11] Ye WY, Efthymiadis P, Pinna C, Ma AX, Shollock B, Dashwood R. Experimental and modelling study of fatigue crack initiation in an aluminium beam with a hole under 4-point bending. Int J Solids Struct 2018;138:87–96. https://doi.org/10.1016/j.ijsolstr.2018.01.001.

[12] Schäfer B, Sonnweber-Ribic P, ul Hassan H, Hartmaier A. Micromechanical modeling of fatigue crack nucleation around non-metallic inclusions in martensitic high-strength steels. Metals 2019;9(12):1258. https://doi.org/10.3390/met9121258.

[13] Brahme AP, Inal K, Mishra RK, Saimoto S. The backstress effect of evolving deformation boundaries in FCC polycrystals. Int J Plast 2011;27(8):1252–66. https://doi.org/10.1016/j.ijplas.2011.02.006.

[14] Dunne FPE, Wilkinson AJ, Allen R. Experimental and computational studies of low cycle fatigue crack nucleation in a polycrystal. Int J Plast 2007;23(2):273–95. https://doi.org/10.1016/j.ijplas.2006.07.001.

[15] Anahid M, Ghosh S. Homogenized constitutive and fatigue nucleation models from crystal plasticity FE simulations of Ti alloys, Part 2: Macroscopic probabilistic crack nucleation model. Int J Plast 2013;48:111–24. https://doi.org/10.1016/j.ijplas.2013.02.008.

[16] Hoshide T, Kusuura K. Life prediction by simulation of crack growth in notched components with different microstructures and under multiaxial fatigue. Fatigue Fract Eng Mater Struct 1998;21(2):201–13.

[17] Repetto EA, Ortiz M. A micromechanical model of cyclic deformation and fatigue-crack nucleation in fcc single crystals. Acta Mater 1997;45(6):2577–95. https://doi.org/10.1016/s1359-6454(96)00368-0.

[18] Robert C, Saintier N, Palin-Luc T, Morel F. Micro-mechanical modelling of high cycle fatigue behaviour of metals under multiaxial loads. Mech Mater 2012;55: 112–29. https://doi.org/10.1016/j.mechmat.2012.08.006.

[19] Bennett VP, McDowell DL. Polycrystal orientation distribution effects on microslip in high cycle fatigue. Int J Fatigue 2003;25(1):27–39. https://doi.org/10.1016/s0142-1123(02)00057-9.

[20] Li Y, Aubin V, Rey C, Bompard P. Polycrystalline numerical simulation of variable amplitude loading effects on cyclic plasticity and microcrack initiation in austenitic

steel 304L. Int J Fatigue 2012;42:71–81. https://doi.org/10.1016/j.ijfatigue.2011.07.003.

[21] Gaur V, Briffod F, Enoki M. Micro-mechanical investigation of fatigue behavior of Al alloys containing surface/superficial defects. Mater Sci Eng A-Struct Mater Propert Microstruct Process 2020;775:138958. https://doi.org/10.1016/j.msea.2020.138958.

[22] Cheong K-S, Smillie MJ, Knowles DM. Predicting fatigue crack initiation through image-based micromechanical modeling. Acta Mater 2007;55(5):1757–68. https://doi.org/10.1016/j.actamat.2006.10.038.

[23] Navarro C, Vázquez J, Domínguez J. 3D vs. 2D fatigue crack initiation and propagation in notched plates. Int J Fatigue 2014;58:40–6. https://doi.org/10.1016/j.ijfatigue.2013.02.024.

[24] Opinsky AJ, Smoluchowski R. The crystallographic aspect of slip in body-centered cubic single crystals. II. Interpretation of experiments. J Appl Phys 1951;22(12): 1488–92. https://doi.org/10.1063/1.1699897.

[25] Nine HD. Slip planes and asymmetric slip in fatigue of iron single crystals. Phil Mag 1972;26(6):1409–18.

[26] Tian C, Dehm G, Kirchlechner C. Influence of strain rate on the activation of 110}, {112}, {123 slip in ferrite of DP800. Materialia 2021;15:100983. https://doi.org/10.1016/j.mtla.2020.100983.

[27] Gillner K, Münstermann S. Numerically predicted high cycle fatigue properties through representative volume elements of the microstructure. Int J Fatigue 2017; 105:219–34. https://doi.org/10.1016/j.ijfatigue.2017.09.002.

[28] Manonukul A, Dunne FPE. High– and low–cycle fatigue crack initiation using polycrystal plasticity. Proc R Soc Lond A 2004;460(2047):1881–903.